Chapter 4

Experimental Validation

In Chapter 2 we introduced a forward model for light transport in scattering tissue. In this chapter we want to compare numerical results of the light transport forward model with experimental data. Experiments were carried out on scattering phantoms using NIR light. The optical parameters of the phantoms were determined by other independent measuring techniques and light transport models. Given the optical parameters of the phantoms within a known error, we compared the outgoing fluence ϕ on the boundary of the phantom with predicted detector readings of the forward model.

4.1 Experimental Set-up

The experimental set-up consisted of three major parts: (a) a solid phantom, (b) a light source, and (c) a light detection system. The light source illuminated the phantom, which was a scattering medium with known optical parameters. The light propagated inside the medium and escaped through the boundaries. A detector measured the outgoing light intensity. The experimental set-up is shown in Figure 4.1.

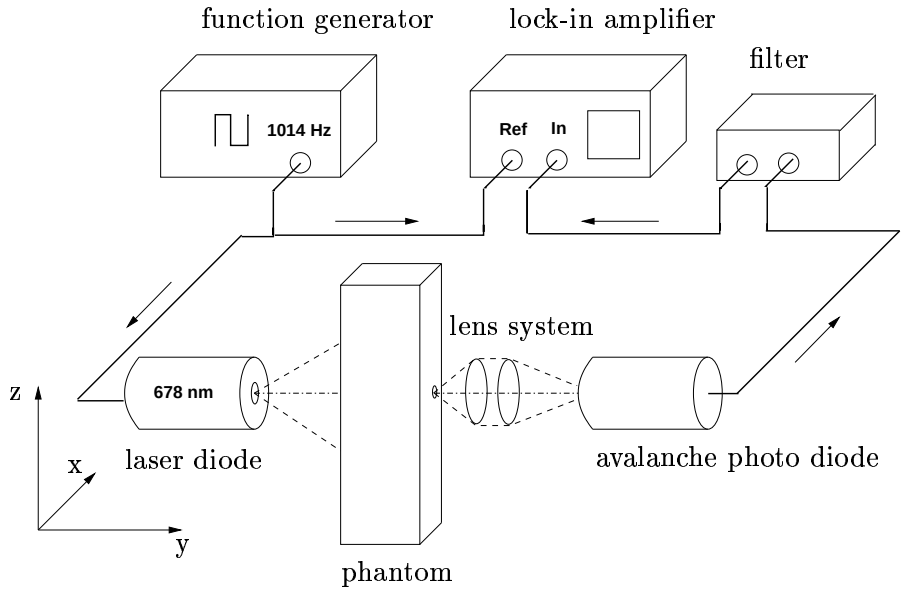

Figure 4.1: Experimental set-up.

4.1.1 Scattering Phantoms

The phantoms were composed of clear epoxy resin into which silicon-dioxide (SiO_2) monospheres and ink were mixed. The scattering properties were adjusted by varying the concentration of the monospheres, while the absorption properties were controlled by the concentration of the ink. The g-factor could be varied by using spheres with different diameters. The optical parameters μ_s, μ_a, and g of the phantom were determined by two different methods at a wavelength of $\lambda = 678$ nm, namely an integrating sphere approach [Pickering92] and a time-resolved transillumination technique [Patterson89].

Using the integrating-sphere approach, a thin slice of the phantom material was illuminated by a collimated laser beam. The collimated, the diffuse, and the reflected light intensities were measured with an integrating sphere. Subsequently, a MC simulation was used to determine the required absorption coefficient μ_a, scattering coefficient μ_s, and the

anisotropy factor g.

The time-resolved transillumination technique measured the time-dependent distribution of the photons that traveled through a 2 cm thick slab of the medium. The transmitted pulse was compared to an analytical solution given by the diffusion equation for a slab geometry. Thus, the reduced scattering coefficient $\mu_s' = (1-g)\mu_s$ and the absorption coefficient μ_a could be determined. Both methods have shown similar results for the reduced scattering coefficient within an error of approximately 3%, but showed larger differences for the absorption coefficient.

Two phantoms were made of scattering material with different optical parameters. First, a 3 cm $\times$ 3 cm $\times$ 14 cm homogeneous phantom was designed (see Figure 4.2(a)), which had a reduced scattering coefficient of $\mu_s' = 11.6 \pm 0.3$ cm^{-1}. The absorption coefficient was determined to be $\mu_a = 0.35 \pm 0.1$ cm^{-1}, with the MC technique giving higher absorption values than the time-resolved slab technique. Using the diameter of monospheres (d = 0.51 μm) and the Mie-Theory for light scattering of spheres [Hulst57] [Bohren83], an anisotropy factor $g = 0.805$ was calculated. This is in agreement with the measurement obtained by the integrating-sphere approach, which provided a value of $g = 0.8 \pm 0.17$. The refractive index of resin is $n = 1.56$ [Firbank93] [Firbank95].

From the same material we fabricated a 4 cm $\times$ 4 cm $\times$ 14 cm phantom that contained a ring with an inner diameter of 2.8 cm and an outer diameter of 3 cm (see Figure 4.2(b)). The ring was oriented along the 14 cm long z-axis of the phantom and was filled with water to mimic void-like regions with low scattering and low absorption.

4.1.2 Light Source

The phantoms were continuously illuminated with near-infrared light from a laser diode (LAS-670-20, Laser 2000 GmbH, Germany) at $\lambda = 678$ nm. As the phantoms were

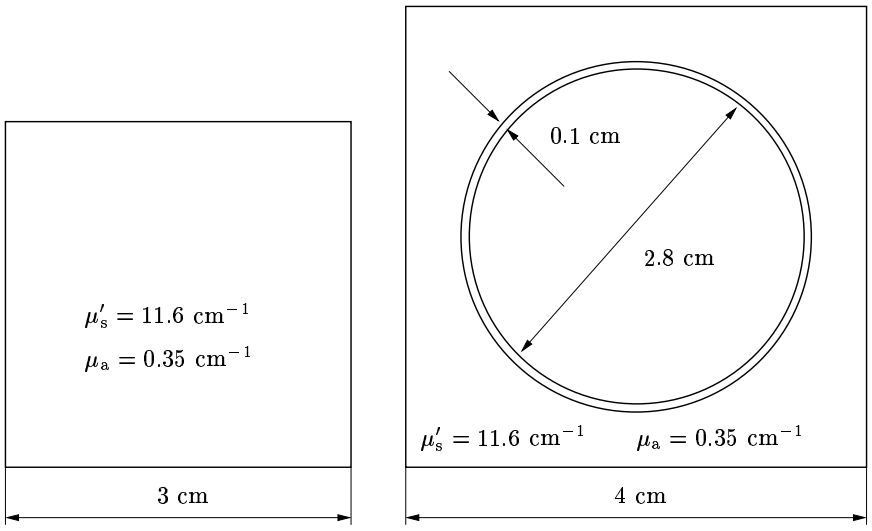

(a) Homogeneous phantom. (b) Phantom with void-like ring.

Figure 4.2: Schematic of phantoms in x-y plane.

three-dimensional but the calculations were two-dimensional, we had to provide a z-axis independent fluence $\phi(\boldsymbol{r} = (x, y, z = \text{const}))$. That was achieved by illuminating the phantom with an extended line source along the z-axis instead of using a point source. The line source was realized by a laser diode with a light emission angle of 20° in the y-z plane, while the beam was collimated in the x-y plane. In this way, the source consisted of a 6 cm long line with a width of 0.1 cm on the surface of the phantom. The source power applied to an area of 0.01 cm^2 was 0.2 ± 0.01 mW. Measurements were taken with the line source positioned at different locations along the x-axis.

4.1.3 Light Detection

We used an avalanche photo diode APD (C5460-01, Hamamatsu, Japan) to measure the fluence $\phi(x, y)$. The APD had a noise equivalent power (NEP) of 0.02 pW Hz$^{-1/2}$

at $\lambda = 800$ nm [1]. The detector was placed in the x-y plane of the phantom at the midpoint of the z-axis ($z = 7$ cm), and could be translated around the phantom along the x-axis and y-axis. The detection area at the boundary of the phantom was limited by a pinhole, which had a diameter of 0.1 cm. Two lenses projected the detection area onto the APD chip, whose diameter was 0.3 cm. An iris was placed in between the lenses, in order to adjust the aperture angle to $45^o \pm 5^o$.

We used a lock-in technique to improve the signal-noise ratio. A function generator (Waveform Generator 33120A, Hewlett Packard, USA) provided a sinusoidal modulation of the laser diode input with a frequency at 1014 Hz. The lock-in amplifier (Model SR 830, Stanford Research Systems, USA) had a time constant of 3 seconds. An active bandwidth filter was connected between detector output and lock-in amplifier input. The working point was at 1014 Hz with a bandwidth of 7 Hz. This efficiently suppressed the noise contributed by other frequencies, especially background light. At one detection spot the measuring time was approximately 10 seconds. During this time the measured fluence varied less than 0.2%. In general, signal levels were reproducible within 1% after removal and reinsertion of the sample into the measurement set-up and realignment of both source and detector. The largest variations were observed for measurement points located close to the corners of the phantom.

4.2 Results

The calculated fluence $\phi(\boldsymbol{r})$ of the forward model was compared to experimental data of the transilluminated scattering phantoms on the accessible surface. We only

[1] The NEP is the amount of light equivalent to the noise level of a device at the operating wavelength. Stated differently, it is the light level required to obtain a signal-to-noise ratio of unity. Since the noise level is proportional to the square root of the frequency bandwidth, the NEP is measured at a bandwidth of 1 Hz and thus expressed in units of W $\text{Hz}^{-1/2}$.

compared relative fluence profiles on the boundary, not absolute fluences. This situation is typically encountered in clinical settings, because of the difficulty in calibrating the measurement system to an accurate absolute value of the source strength [Boas01]. The exact absolute value is difficult to determine because of the unknown coupling coefficients between the skin and the sources or detectors. Thus, the measurement data and simulated data were normalized by their mean value of all D detector readings ϕ_d of each source to provide relative fluence profiles independent of its source strength (see Equation 3.1 on page 42). The fluence ϕ_d of the d-th detector in Equation 3.1 can be either a measurement value m_d or a predicted detector reading p_d. This procedure of normalizing the fluence of the detector readings $\boldsymbol{m}$ and predictions $\boldsymbol{p}$ is carried out throughout this entire work.

4.2.1 Homogeneous Phantom

First, we compared the measured and predicted fluence profiles of the homogeneous phantom. The numerical calculations with the upwind-difference discrete-ordinates method were performed on a 181×181 grid, with $\Delta x = \Delta y = 0.0167$ cm $\approx 1/\mu_s$. 32 discrete ordinates were used for each calculation. The aperture of the APD detector was 45^o in the x-y plane. Therefore, the radiance at the boundary in the simulation was summed over 4 ordinates. The overrelaxation parameter was $\rho = 1.15$. The calculated fluence was compared to the measured data on the boundary of the phantom. The source was placed at three different positions (A: 0.3 cm, B: 0.9 cm, and C: 1.5 cm from the edge of the phantom). For each source position measurements were taken along the side opposite to the source (x-axis) and the side adjacent to the source (y-axis). The separation between measurement points was 0.1 cm, resulting in 28 measurement points on each side. Figure 4.4 shows the experimental data and numerical calculations for the three different source positions. In Figure 4.4(a) the results along the side opposite to the source are presented (x-axis), and

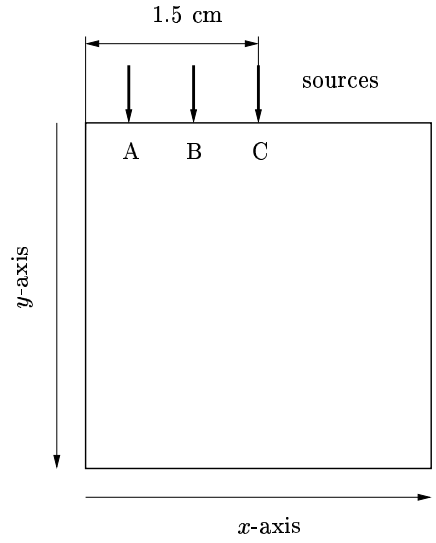

Figure 4.3: Source and detector positions of the homogeneous phantom. Sources: (A) 0.3 cm, (B) 0.9 cm, and (C) 1.5 cm from the edge of the phantom.

Figure 4.4(b) shows the results for the adjacent side (y-axis). The measurement error is not displayed because the error bars are smaller than the circles and diamonds in the figures.

To investigate how the predictions of the forward model depend on the variations in optical properties, we studied the sensitivity of the numerical predictions to changes in the scattering coefficient, the absorption coefficient, and the anisotropy factor. We compared the calculated fluence with the measured fluence along the x-axis and y-axis for source position C (Figures 4.5 and 4.6). In Figure 4.5(a), numerical results are shown for the case of a fixed reduced scattering coefficient $\mu_s' = (1-g)\mu_s$, but varying μ_s and g-factor. Figure 4.5(b) displays results for different μ_s while all other parameters (μ_a and g) were kept constant. The absorption coefficient was varied in Figure 4.5(c). The anisotropy factor was varied in Figure 4.5(d). The same study was done on the y-axis (Figure 4.6).

To evaluate the degree of agreement between numerical data $\boldsymbol{p}$ and experimental

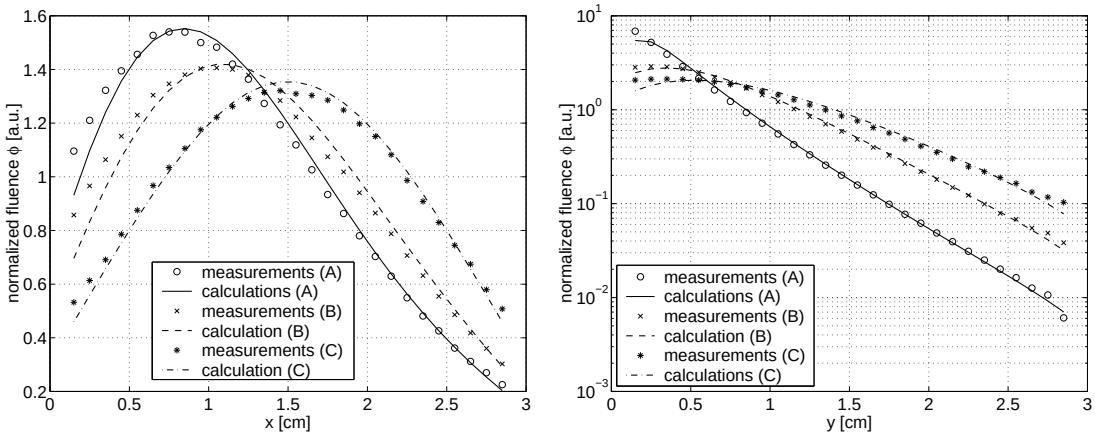

(a) Detectors along the x-axis.

(b) Detectors along the y-axis.

Figure 4.4: Relative fluence ϕ for different source positions A, B, and C of the homogeneous phantom.

data $\boldsymbol{m}$, we calculated for each set of data the average error for D detector points given by

$$R = \frac{100}{\mathrm{D}} \sqrt{\sum_{\mathrm{d}}^{\mathrm{D}} \frac{(m_{\mathrm{d}} - p_{\mathrm{d}})^2}{m_{\mathrm{d}}^2}}. \tag{4.1}$$

The R-value is calculated separately for the x-axis data and y-axis data. Therefore, the sum in Equation 4.1 is taken over all detector readings along one side for one source. Table 4.1 shows the R-values for all source positions A, B, and C. The average error between numerical and experimental data varies from 0.47% to 63%. For comparison, the average differences between two measurements on the same phantom with the same source-detector configuration are typically less than 0.2% along the side opposite to the source (x-axis), and less than 1% along the side adjacent to the source (y-axis).

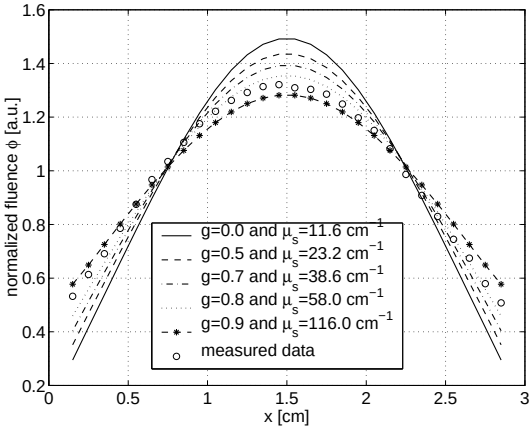

(a) Anisotropy factor and scattering coefficient were varied (μ_s' was constant).

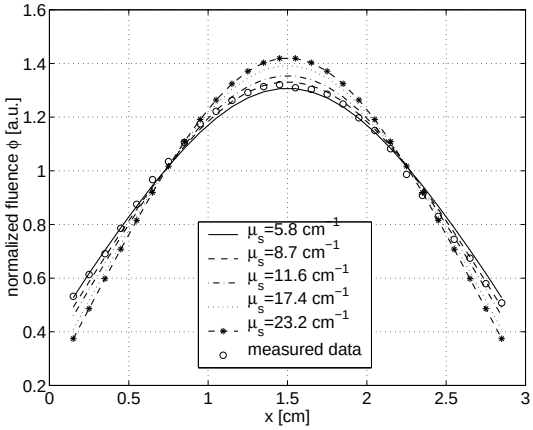

(b) Scattering coefficient was varied.

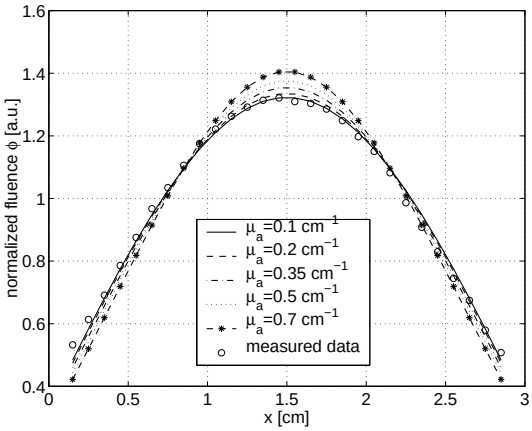

(c) Absorption coefficient was varied.

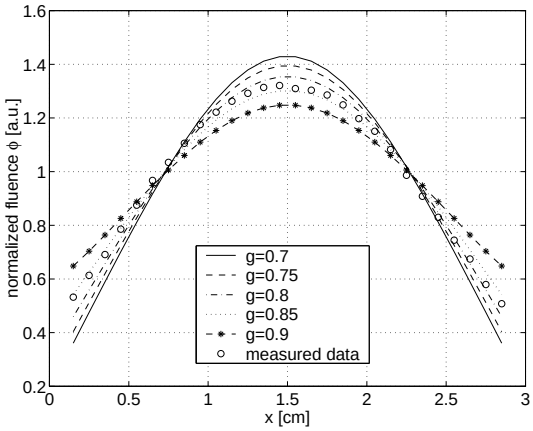

(d) Anisotropy factor was varied.

Figure 4.5: Relative fluence $\phi(x)$ along the x-axis for source position C. Different optical parameters were varied.

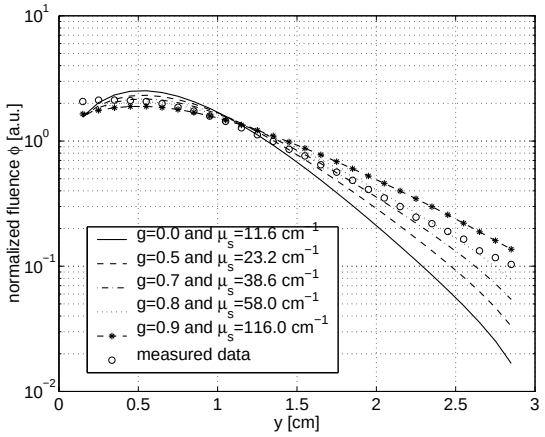

(a) Anisotropy factor and scattering coefficient were varied (μ_s' was constant).

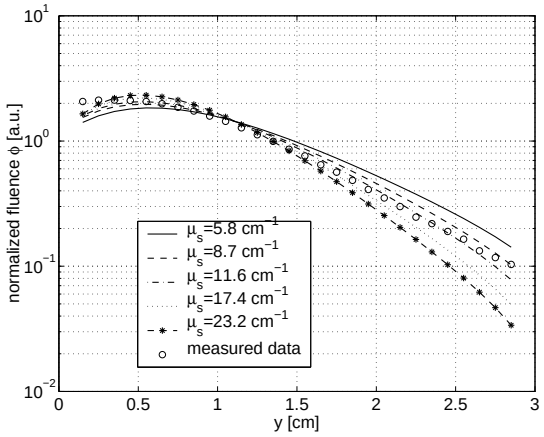

(b) Scattering coefficient was varied.

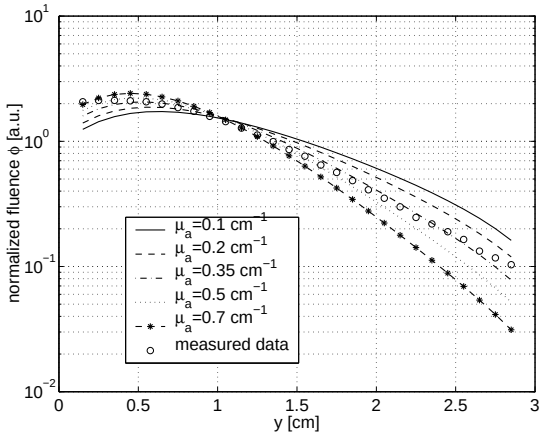

(c) Absorption coefficient was varied.

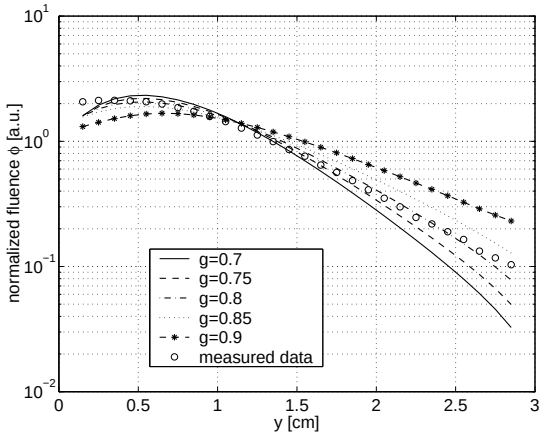

(d) Anisotropy factor was varied.

Figure 4.6: Relative fluence $\phi(y)$ along the y-axis for source position C. Different optical parameters were varied.

data taken along: source position:	x-axis A	x-axis B	x-axis C	y-axis A	y-axis B	y-axis C
($\mu_s' = 11.6$ cm^{-1}, $\mu_a = 0.35$ cm^{-1}):						
($\mu_s = 11.6$ cm^{-1}, $g = 0.0$)	3.27	3.78	4.97	7.83	9.79	12.81
($\mu_s = 23.2$ cm^{-1}, $g = 0.5$)	2.35	2.51	3.1	5.39	6.96	10.02
($\mu_s = 38.6$ cm^{-1}, $g = 0.7$)	1.57	1.66	1.79	3.17	3.77	5.87
($\mu_s = 58$ cm^{-1}, $g = 0.8$)	0.82	1.15	0.9	1.83	1.17	1.42
($\mu_s = 116$ cm^{-1}, $g = 0.9$)	0.98	1.74	1.47	4.46	7.74	18.14
($\mu_a = 0.35$ cm^{-1}, $g = 0.8$):						
($\mu_s' = 5.8$ cm^{-1})	0.51	1.43	1.24	5.93	9.52	21.95
($\mu_s' = 8.7$ cm^{-1})	0.47	1.2	0.85	2.79	3.67	7.11
($\mu_s' = 11.6$ cm^{-1})	0.82	1.15	0.9	1.83	1.17	1.42
($\mu_s' = 17.4$ cm^{-1})	1.51	1.6	1.89	3.68	4.58	6.75
($\mu_s' = 23.2$ cm^{-1})	2.03	2.2	2.9	5.44	6.97	9.75
($\mu_s = 58$ cm^{-1}, $g = 0.8$):						
($\mu_a = 0.1$ cm^{-1})	0.53	3.02	4.34	9.01	13.65	22.82
($\mu_a = 0.2$ cm^{-1})	0.62	2.11	2.58	4.9	6.58	10.10
($\mu_a = 0.35$ cm^{-1})	0.82	1.15	0.9	1.83	1.17	1.42
($\mu_a = 0.5$ cm^{-1})	1.08	1.15	2.01	3.59	4.31	5.6
($\mu_a = 0.7$ cm^{-1})	1.47	2.1	3.97	6.23	7.57	9.38
($\mu_s = 58$ cm^{-1}, $\mu_a = 0.35$ cm^{-1}):						
($g = 0.7$)	2.22	2.4	3.05	5.53	7.12	10.09
($g = 0.75$)	1.58	1.67	1.93	3.61	4.48	6.73
($g = 0.8$)	0.82	1.15	0.9	1.83	1.17	1.42
($g = 0.85$)	0.59	1.47	1.2	4.29	6.96	15.47
($g = 0.9$)	1.88	2.44	2.48	11.5	20.57	63.33

Table 4.1: Average error R [%] of the predicted fluence profiles with respect to the measured fluence profiles.

4.2.2 Phantom with Void Ring

The results of measurements and predictions for the phantom, which contained a water-filled ring are shown in Figure 4.8. The forward calculations were done on a 241×241 grid, with a grid point separation of $\Delta x = \Delta y = 0.0167$ cm and 32 ordinates. Measurements were taken along the x-axis and y-axis at 38 detector points, with a spacing of 0.1 cm. The sources were located at three different points (A: 0.4 cm, B: 1.2 cm, and C: 2 cm from the edge of the phantom), see Figure 4.7.

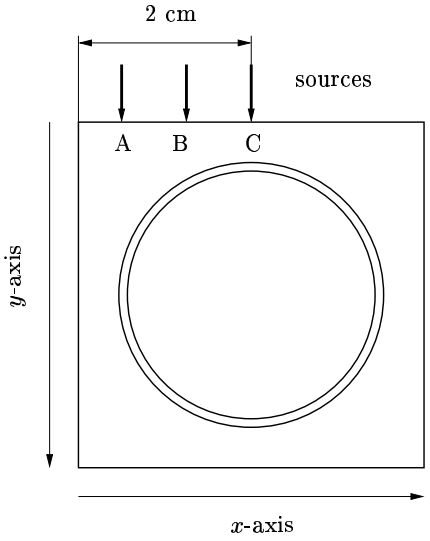

Figure 4.7: Source and detector positions of the phantom with a void-like ring. Sources: (A) 0.4 cm, (B) 1.2 cm, and (C) 2 cm from the edge of the phantom.

4.3 Discussion

Overall, we observed good agreement between measurements and the calculations based on the assumed, independently verified, optical properties. For the homogeneous phantom we found that the average error between the measured and calculated data for $\mu_s = 58$ cm^{-1}, $g = 0.8$, and $\mu_a = 0.35$ cm^{-1} was between 0.82% and 1.83% for various source

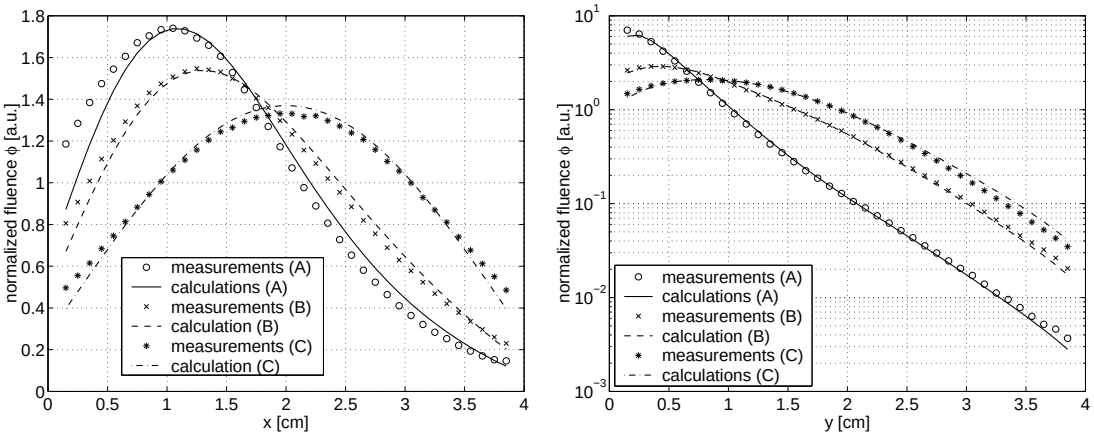

(a) Detectors along the x-axis.

(b) Detectors along the y-axis.

Figure 4.8: Relative fluence ϕ for different source positions A, B, and C of the phantom with void-like ring.

detector configurations (Figure 4.4). This error increases if other sets of optical properties are used as parameters for the forward code.

Several key observations can be made when evaluating the sensitivity of the predicted data for the homogeneous phantom to changes in the optical properties. For example, we found that the data along the y-axis are more sensitive to changes in optical properties than data along the x-axis. As can be seen in Table 4.1, the error R between the calculated and measured data is consistently higher for data sets taken along the y-axis of the phantom as compared to data sets taken along the x-axis of the phantom. This suggests that for the successful reconstruction of optical parameters it is advantageous to employ not only transmitted intensities of the target medium, but also to include measurements on the sides of the object.

The importance of exact knowledge of both μ_s and g to characterize homogeneous media is illustrated in Figures 4.5(a) and 4.6(a). In these graphs, $\mu_s' = (1-g)\mu_s$ is fixed and different combinations of g and μ_s are used in the calculations of the fluence distribution.

It can be seen that only one combination ($\mu_s = 58$ cm^{-1} and $g = 0.8$) fits the data well. In algorithms that use the diffusion approximation to the ERT only the parameter μ_s' appears as independent variable. However, all combinations of μ_s and g yield the same μ_s', yet the results are not the same (see Figures 4.5(a) and 4.6(a)).

For the phantom with the void like ring the average error R was between 0.81% and 4.43% for all source-detector configurations. This experimentally confirms our previous findings that, unlike diffusion-theory-based codes, forward models based on the ERT can accurately describe the light propagation in media that contain void-like regions [Hielscher98].

While good overall agreement between measurement and simulated data was found, some differences remain. There appear to be two main reasons for this. First, the experimental determination of the optical properties of the phantom that was used to validate the numerical forward model is subject to errors. Different methods, such as single integrating sphere, double integrating sphere, time-resolved technique, time-independent methods, etc., all have advantages and disadvantages and often lead to different answers. For example, over the last 15 years several groups have measured the optical properties of INTRALIPID®, which is a milk-like emulsion of fat particles [Star87] [Moes89] [Staveren91]. Flock *et al* summarizes these studies by giving the means and standard deviations of all works combined. They find that the optical properties of 10% INTRALIPID® at 633 nm are $\mu_a = 0.027 \pm 0.154$ cm^{-1}, $\mu_s' = 144 \pm 9$ cm^{-1}, and $g = 0.75 \pm 0.18$ [Flock92]. Therefore, in agreement with our observation they find that μ_a values differ strongly from method to method, while μ_s' is determined rather consistently. Unfortunately, no single technique has been accepted within the biomedical optics community as a standard for measuring optical properties. Therefore, the validation of any algorithms remains somewhat uncertain, especially with respect to μ_a.

Second, the upwind-difference discrete-ordinates method used in this work, is like any other numerical method an approximation to the ERT. In this case the spatial variable is

discretized to the first-order. Higher-order discretization that yield more complex algorithms may further improve the match between the experimental and measured data.